Optimization of a fluorine-free metal-organic deposition to fabricate BaZrO₃-doped YBa₂Cu₃O₇₋δ film on RABiTS substrates

F Lu[1], F Kametani and E E Hellstrom

Applied Superconductivity Center, National High Magnetic Field Laboratory, Tallahassee, FL 32310, USA

E-mail: fenglu@physics.tamu.edu

Abstract

In this study, we used a systematic route to optimize the fluorine-free MOD process to achieve a high critical current density (J_c) in BaZrO₃ (BZO)-doped YBCO films on RABiTS substrates. The BZO content is given by 1 YBCO + x BZO films, where x is moles of BZO per 1 mole of YBCO. We found $x = 0.10$ to be the optimal BZO content and ∼795–805 °C to be the optimal growth temperature window with 60–90 min processing time. TEM studies show the BZO nanoparticles are ∼20 nm in size and spaced ∼50–100 nm apart. The in-field J_c and the peak pinning force (F_p) of the film grown at the optimal conditions were greatly increased at 77 K relative to pure YBCO films, achieving ∼6.7 GN m⁻³ at 77 K, $H \parallel c$ in a ∼800 nm thick $x = 0.10$ film. The angular dependence of in-field J_c measurements also shows greatly reduced angular anisotropy at 1 and 4 T at 77 K due to isotropic pinning by BZO nanoparticles.

(Some figures may appear in colour only in the online journal)

1. Introduction

YBa₂Cu₃O₇₋δ (YBCO) coated conductor (CC) is one of the most promising materials for many technological applications of high-T_c superconductors (HTS), since they have high critical current densities (J_c) in a magnetic field at 77 K [1]. Several distinct methods have been developed to enable continuous deposition of biaxially textured YBCO films onto long-length flexible metallic substrates including rolling-assisted biaxial textured substrates (RABiTS) [2, 3] and ion-beam-assisted deposition (IBAD) [4]. Metal-organic deposition (MOD) is suitable for mass production of large-area films at low cost without using high-vacuum systems. The trifluoroacetate (TFA) route is an MOD method to produce YBCO thin films with high J_c [5, 6] for CCs [3].

The standard TFA method uses water to decompose the BaF₂, producing highly corrosive and toxic HF gas as a by-product, which is of environmental concern, especially for large-scale production. It is therefore of interest to develop solution processes where HF evolution is eliminated or greatly reduced. There are some low-fluorine [7, 8] and fluorine-free (F-free) precursors [9–14] that have been prepared for this purpose. One of these F-free processes is an acetylacetonate (AcAc) solution-based MOD technique, originally developed by the National Institute of Advanced Industrial Science and Technology (AIST) [15–17] and used by Sumitomo Electric Industries [18]. The F-free MOD approach is applicable on the same templates and substrates used for other MOD YBCO film deposition techniques, so it is a potential alternative for scaling up low-cost, long-length coated conductors on RABiTS or IBAD substrates.

Although 1,000 m long CC has been demonstrated with a minimum critical current (I_c) of ∼300 A cm⁻¹ and

---

[1] Present address: Department of Physics and Astronomy, Texas A&M University, College Station, TX 77843, USA.

100–300 m CCs are commercially available [19], there are still major challenges to use CC in many applications due to the dramatic reduction of J_c in moderate-to-high magnetic fields and the angular dependence of J_c in a magnetic field. To improve the in-field performance of YBCO CC, it is important to enhance pinning in YBCO films. Flux pinning in YBCO is accomplished by intrinsic and extrinsic defects. The most effective pinning occurs when the size of defects is in the range of the superconducting coherence length and the defects are uniformly distributed in the superconductor [20]. Enormous strides have been made in engineering nanoscale defects in YBCO films. BaZrO$_3$ (BZO), which has the perovskite structure, is one of the most extensively studied nano-size additions to achieve strong pinning in YBCO films. Self-assembled BZO nanorods can be grow *in situ* in films deposited using pulsed laser deposition (PLD) and metal-organic chemical vapor deposition (MOCVD) [4, 21–23]. BZO nanoparticles have also been successfully introduced into YBCO films by the *ex situ* TFA-MOD method using Zr-doped precursor solutions [2, 5, 6]. In the *ex situ* TFA-MOD process, the precursor film containing the cations is coated onto the substrates at room temperature and then converted to a YBCO + BZO composite structure by subsequent heating. In all these studies, the pinning force is found to be significantly increased by BZO doping compared to pure YBCO films. Here we present work using the *ex situ* F-free MOD route to grow BZO-doped YBCO films on metallic RABiTS substrates.

We have previously used the F-free MOD process to deposit BZO-doped YBCO thin film (200–300 nm) on (100)-oriented single crystal SrTiO$_3$ (STO) and demonstrated a very high pinning force of $\sim$10 GN m^{-3} at 77 K, $H \parallel c$ [24]. The motivation of the present study was to deposit $\sim$1 μm thick, high-J_c YBCO film on commercial RABiTS substrates using the same AcAc-based F-free MOD approach and to enhance its in-field performance by forming BZO nanoparticles in the YBCO matrix. Here we report on our systematic study of forming BZO-doped YBCO film on RABiTS substrates using the F-free MOD process.

2. Experimental procedures

The F-free precursor solutions were prepared by dissolving Y-, Ba-, and Cu–AcAc (Alfa Aesar) in a Y:Ba:Cu 1:2:3 mole ratio in a mixture of pyridine (PY) and propionic acid (PA) (PY:PA = 5:3 by volume) at room temperature. BZO-doped YBCO was made by adding Zr–AcAc and extra Ba–AcAc in a 1:1 Ba:Zr mole ratio to achieve an overall stoichiometry given by 1 YBCO + x BZO, where x is the moles of BZO per 1 mole of YBCO. Films with $x = 0$–0.15 were synthesized. The exact degree of AcAc hydration was measured by heating a small amount of each AcAc powder in flowing air in a combination thermogravimetric plus differential thermal analysis system (TGA/DTA, TA Instruments 2960 SDT).

After the AcAcs were dissolved, the solution was heated to 70–80 °C in air to evaporate most of the solvents. This yielded a black, tar-like residue that was subsequently dissolved into methanol, forming a homogeneous dark-green

solution. It has been shown that polyethylene glycol (PEG) additive in both TFA [25] and F-free [26] solutions can increase the viscosity and ameliorate the coating performance, leading to a thick YBCO layer with a single deposition on single-crystal substrates. In this study, polyethylene glycol 8000 (PEG-8000) (Alfa Aesar) was added into methanol-based coating solution and the mass of PEG-8000 was $\sim$10–15 wt%. The total metal cation concentration in the final solution was adjusted to be $\sim$1 M. Inductively coupled plasma-atomic emission spectrometry (ICP-AES) was used to determine the individual cation concentrations. The buffered RABiTS substrates (CeO$_2$/YSZ/Y$_2$O$_3$/NiW from American Superconductor Corp., AMSC) were cut into 10×10 mm^2 pieces. Just before being mounted onto the stage of a photoresist spin coater, the substrate was cleaned by successive acetone and methanol ultrasonic baths for about $\sim$10 min and then dried in a stream of Ar or N$_2$. The precursor solution was then dropped onto the clean RABiTS substrate to cover the whole surface using a syringe. Then the substrate was spun at $\sim$4000 rpm for 60 s. The precursor film was decomposed after spinning, following the procedure in [24]. The coating and decomposition steps were repeated three times to increase the final film thickness to $\sim$0.8–1 μm. The precursor films were converted to superconducting films in three steps: decomposition, reaction, and oxygenation, as described previously [24]. The decomposed precursor films were initially processed at 775 °C for 60 min in a flowing Ar atmosphere containing 150 ± 50 ppm oxygen, followed by an oxygenation treatment at 500 °C in 1 bar flowing oxygen for 2 h to convert the tetragonal YBCO phase to the superconducting orthorhombic phase and oxygenate the samples.

Through-process quench experiments were performed to investigate the formation of BZO and YBCO and determine the optimal processing time. A horizontal quench furnace was built with a quartz muffle tube that was asymmetrically placed in the furnace so one end stuck a long ways out of the furnace and was close to room temperature when the furnace was at 805 °C. To quench a sample after the desired processing time at 805 °C, the sample was quickly pulled out of the center of the furnace towards the cold end of the quartz tube and the quartz setter plate the sample was sitting on was swiftly turned upside down dropping the sample on the room temperature wall of the quartz tube, quenching the small sample to room temperature. All quenched films were subsequently annealed at 500 °C in pure oxygen for 2 h.

The surface and cross-section morphology of the films was investigated using a Carl Zeiss 1540EsB/XB Field Emission SEM with a focused ion beam (FIB). A transmission electron microscope (TEM) study was carried out using a JEOL JEM2011 microscope. X-ray diffraction (XRD) data were obtained using a PANalytical X'Pert diffractometer (Cu Kα). The sample resistance (R) and critical current (I_c) were measured with a four-point configuration at 77 K in magnetic fields up to 9 T with the field perpendicular to the film surface ($H \parallel c$; 9 T Quantum Design Physical Property Measurement System (PPMS) and a home-built 1 T electromagnet system). We cut bridges $\sim$120 μm wide and

Table 1. Summary of T_c, and J_c(SF), F_p^{max} and H_{irr} (77 K) for 1 YBCO + x BZO films on RABiTS processed at 775 °C for 60 min.

	BZO content					
x	Mol%	Vol%	T_c (K)	J_c(SF, $H \parallel c$) (MA cm^{-2})	H_{irr} (T)	Maximum F_p (GN m^{-3})
0	—	—	90.8	2.75	6.3	2.0
0.07	6.54	3.26	88.5	2.59	6.9	3.9
0.10	9.09	4.60	88.2	2.65	7.5	5.1
0.12	10.71	5.46	88.0	2.40	7.4	4.7
0.15	13.04	6.73	86.9	1.73	6.4	2.0

~500 μm long in the films using a Nd–YAG laser (Amoco Laser Co.) to restrict I_c to <3 A to prevent the samples from overheating. I_c was determined at an electric field criterion of 1 μV cm^{-1}. Angular-dependent J_c measurements were performed by rotating the sample relative to the magnetic field, with the field always normal to the current.

3. Results

3.1. Optimizing the BZO content

Pure and BZO-doped YBCO (x = 0, 0.07, 0.10, 0.12, and 0.15) films were deposited on RABiTS substrates using our F-free MOD process [24]. XRD θ–2θ scans of these films are shown in figure 1(a). As can be clearly seen, two peaks from BZO, (110) at 30.1° and (200) at 43.1°, are observed for all BZO-doped films, which is direct evidence that BZO phases formed in the YBCO film. The relatively weak intensity of the BZO peaks is due to the small volume fraction of BZO, small BZO particle size, and random BZO orientation. Although strong YBCO (00*l*) peaks exist in all the patterns, for x = 0.12 and 0.15 there are also small (103), (200), and (116) YBCO peaks that indicate some degree of texture degradation. There are also some small peaks from BaCeO$_3$, NiO, and NiWO$_4$, which are common for MOD YBCO films deposited on RABiTS due to the reactions between the YBCO and the substrate and buffer layers during the high-temperature process.

FWHM measurements of the YBCO (006) rocking curve and the φ-scan of the (103) YBCO pole are plotted as a function of the BZO content in figure 1(b). The FWHM of the (006) rocking curve for the x = 0.10 film is ~5.1°, which is only 0.4° larger than that from the CeO$_2$ (002) in the buffer layer, which is ~4.7°. The same film shows the FWHM of the peaks of YBCO (103) φ-scan is ~6.2°, which is only 0.3° greater than that of the CeO$_2$ (111) φ-scan, ~5.9°. The small FWHM values confirm the low degree of mosaicity and the high degree of biaxial texture of these YBCO films. For the x = 0.15 film, the YBCO (200) peak is very strong, comparable in intensity to the strongest YBCO (006) peak, indicating severe texture degradation.

The surface microstructures of YBCO films with different BZO doping content are shown in figure 2. All films, except x = 0.12, show smooth and dense surface morphology. The flat features are the typical *c*-axis oriented YBCO grains from the MOD process. The terrace surface structure with some outgrowths and a few voids are common characteristics of
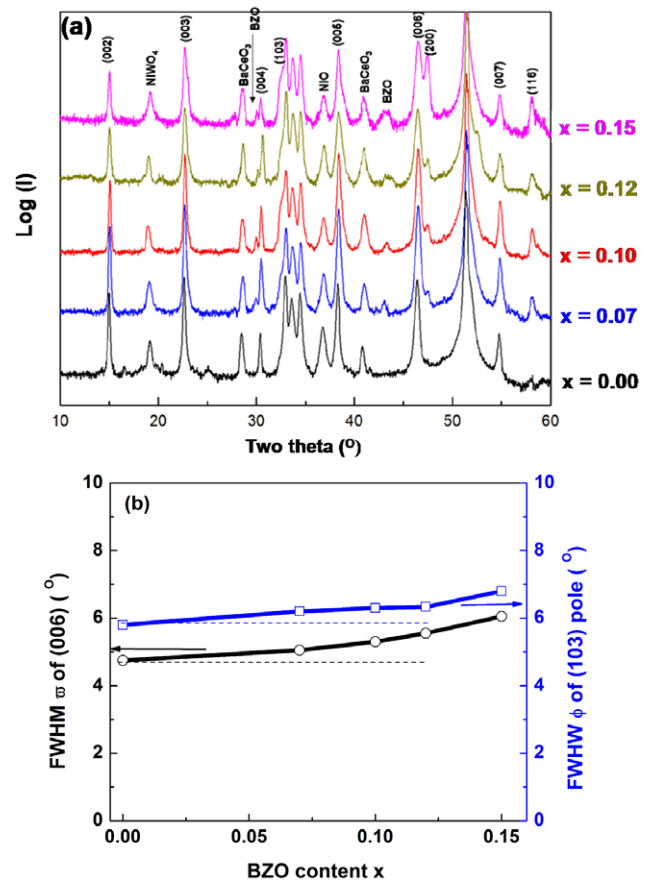

Figure 1. (a) XRD θ–2θ patterns of pure and four BZO-doped YBCO films on RABiTS processed at 775 °C for 60 min. (b) FWHM values of the YBCO (006) rocking curve and YBCO (103) φ-scan. Dashed lines are the reference FWHMs of the CeO$_2$ buffer layer.

solution-derived films [10, 12]. When the BZO content $x \geq$ 0.12, the YBCO film displays large holes and a rough surface that may decrease the grain connections and homogeneity of the YBCO phase.

The measured electromagnetic data for these films are summarized in table 1. The T_c of BZO-doped films is found to be slightly reduced (between 86.9 and 88.5 K) compared to pure, F-free MOD YBCO films, which are routinely made with T_c higher than 90 K on both single-crystal STO and RABiTS substrates. Despite the lowered T_c from BZO doping, the transition width, ΔT_c (defined by $T_c^{onset} - T_c^{offset}$), is found to still be narrow and less than 1.5 K, independent of the BZO content. Figure 3 displays J_c as a function of

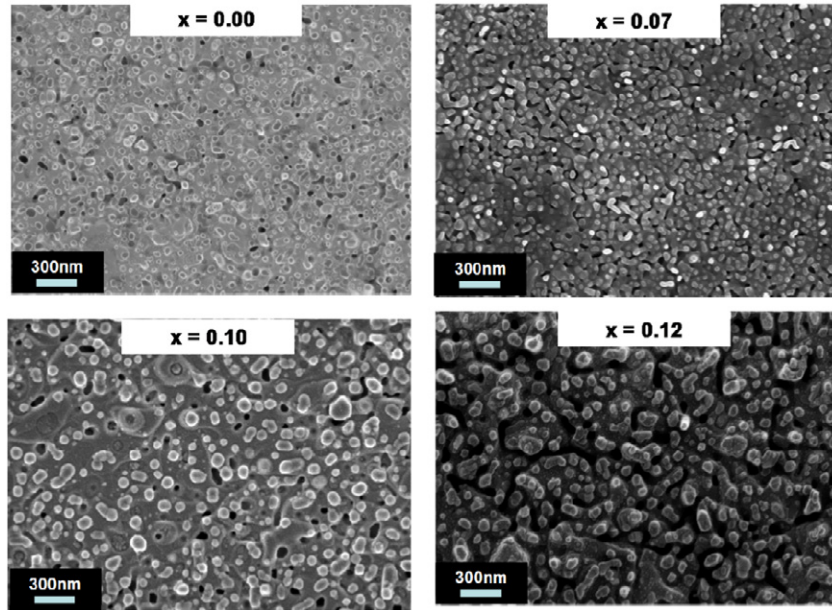**Figure 2.** Surfaces of YBCO films with $x = 0$, 0.07, 0.10, and 0.12 on RABiTS processed at 775 °C for 60 min.

applied magnetic field H, for pure and BZO-doped films. The films with $x = 0.00$–0.12 have self-field (SF) J_c ranging from 2.4 to 2.7 MA cm^{-2} with $H \parallel c$, whereas J_c drops to 1.7 MA cm^{-2} for the $x = 0.15$ film. J_c in the BZO-doped films decreases slower with increasing magnetic field than in the pure YBCO film. The film with $x = 0.10$ has the highest J_c in all fields, while in-field J_c enhancement decreases for films with $x > 0.10$. The irreversibility field H_{irr} of the films, determined using the 100 A cm^{-2} criterion, increased from ~6.3 T for pure YBCO to ~7.5 T for the $x = 0.10$ film, and then decreased back to 6.4 T for the $x = 0.15$ film. The volume pinning force F_p ($= J_c \times H$) was calculated from J_c–H data in figure 3 and the maximum F_p is listed in table 1. The maximum F_p is for the $x = 0.10$ film, which is ~5.1 GN m^{-3} for $H \parallel c$. This is ~2.8 times greater than for pure YBCO film.

Based on these results, $x = 0.10$ was selected as the optimum BZO content in the films and was used for further optimization.

3.2. Optimizing the processing temperature

As in our previous F-free MOD studies [24], we varied the processing temperature to see if it needed to be modified with the $x = 0.10$ addition. We began at 775 °C, which was the previously optimized temperature for pure YBCO, and used 785, 795, 800, 805, 810, and 815 °C, holding the other processing parameters the same as described in section 2.

The XRD patterns in figure 4(a) show that the texture of the $x = 0.10$ films improves with increasing processing temperature from 775 to 810 °C as indicated by the decreasing intensities of the (103), (200), and (116) peaks. For the films grown at 795 and 810 °C, the (103) and (200) peaks are almost negligible, indicating excellent texture in these two films. At 815 °C the texture starts to degrade, which we believe is due to degradation of the buffer layers and the interaction
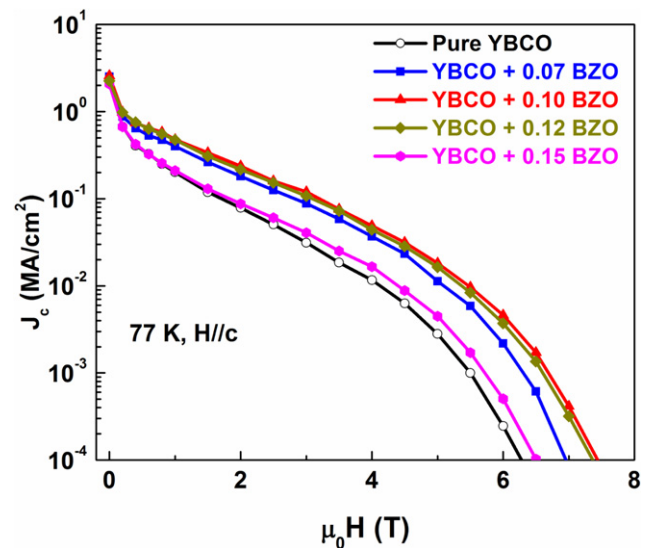

Figure 3. J_c–H at 77 K, $H \parallel c$, for $x = 0.00$, 0.07, 0.10, and 0.15 films on RABiTS processed at 775 °C for 60 min.

between the YBCO, buffer layers, and substrate at this higher temperature. The measured FWHM values of the YBCO (006) ω-scan and YBCO (103) φ-scan are plotted in figure 4(b). As can be seen, there is a significant improvement of both out-of-plane and in-plane textures of the films processed over the temperature range from 795 to 810 °C and these films even have better texture than the CeO$_2$ layer.

Figure 4(c) shows the surface microstructure of the $x = 0.10$ film grown at 805 °C, which is denser and smoother than the film grown at 775 °C (figure 2 for $x = 0.10$). All the YBCO grains are flat and c-axis oriented, consistent with the XRD results showing the texture improvement.

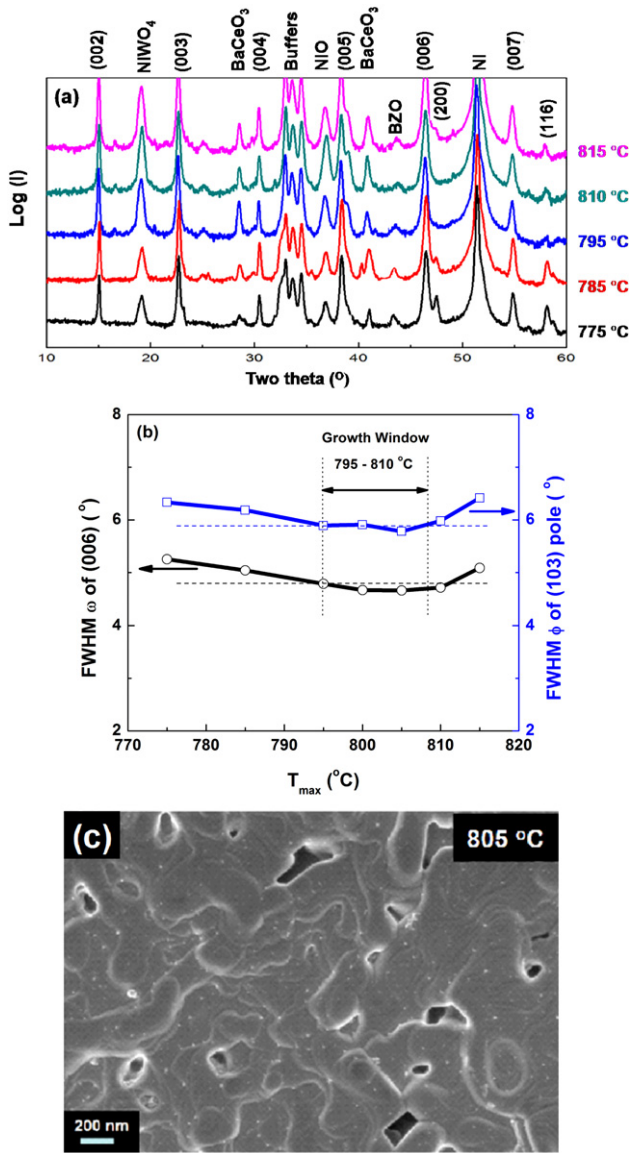Figure 5 displays J_c–H data for applied fields up to 1 T for $x = 0.10$ films processed from 775 to 815 °C. From

Figure 5. J_c–H at 77 K, $H \parallel c$, for $x = 0.10$ films on RABiTS grown at different temperatures.
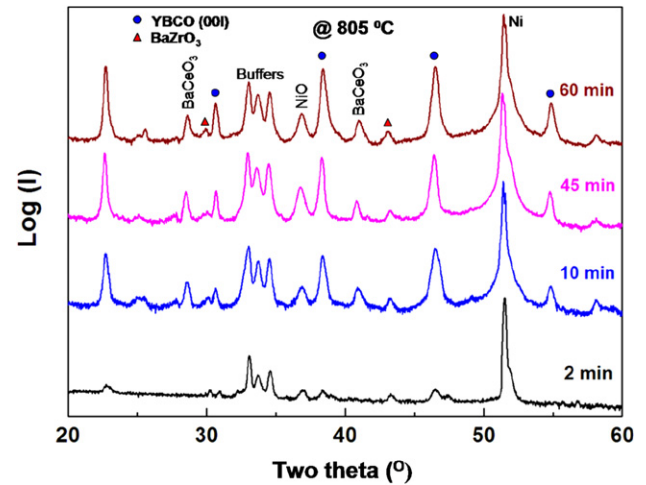
Figure 6. XRD θ–2θ patterns of $x = 0.10$ films on RABiTS at 805 °C quenched after different times at 805 °C.

Figure 4. (a) XRD θ–2θ patterns of $x = 0.10$ films on RABiTS at different growth temperatures. (b) FWHM values of the YBCO (006) rocking curve and YBCO (103) ϕ-scan. Dashed lines are reference FWHMs of the CeO$_2$ buffer layer. (c) Surface of $x = 0.10$ film grown at 805 °C for 90 min on RABiTS.

figure 5, J_c values are significantly enhanced with increasing processing temperature up to 795–805 °C at fields up to 1 T. The 795, 800, and 805 °C films show very similar in-field J_c performance and have the highest J_c. Above 805 °C, J_c decreases and the 815 °C film shows the lowest J_c values at all fields.

Based on these results we chose 805 °C as the optimum processing temperature.

3.3. Optimizing the processing time

To find the optimum processing time and understand the growth mechanisms of both BZO and YBCO, we did through-process quench studies to investigate the evolution of phases, textures, T_c, and J_c of $x = 0.10$ films grown at
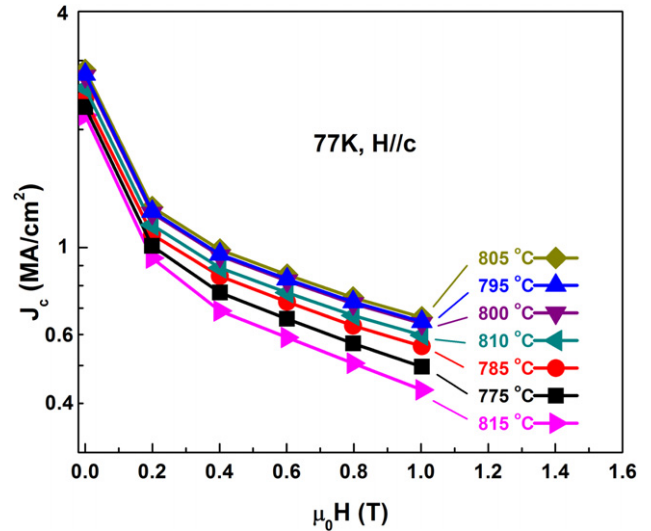
805 °C on RABiTS substrates. The samples were quenched after processing for 2, 5, 10, 20, 30, 45, 60, 90, 120, 180, and 240 min at 805 °C then oxygenated, as described above.

Figure 6 shows the XRD patterns of films quenched at 2, 10, 45, and 60 min. There were peaks for both YBCO and BZO in the 2 min film, though the peaks are weak. With increasing processing time the YBCO peaks become stronger and (00l) peaks start to dominate. In contrast, the BZO peaks at $2\theta \sim 30.1°$ and $\sim 43.1°$ remain about the same as in the 2 min sample. BaCeO$_3$ peaks appear with increasing time due to a reaction between the YBCO and the CeO$_2$ cap layer, and oxygen penetration through the buffer layer to the substrate causes the NiO peak. As mentioned before, BaCeO$_3$ and NiO are typical secondary phases on buffered RABiTS substrates in both F-free and TFA-MOD films. The $x = 0.10$ film is fully textured after 60 min at 805 °C and no further texture improvement is observed for films processed for longer times.
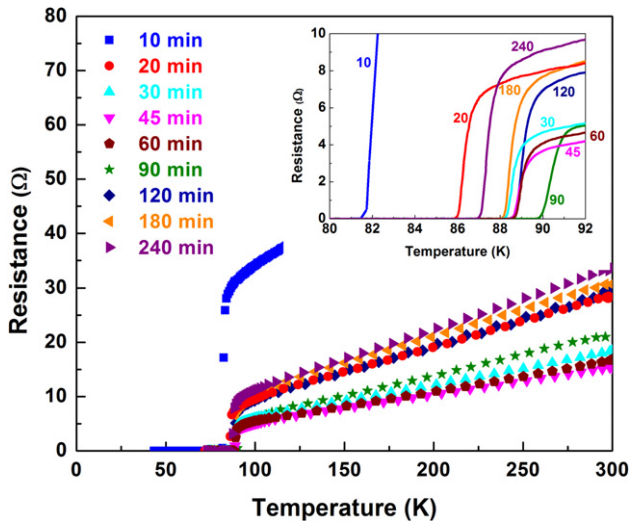
Figure 7. *R–T* plots for *x* = 0.10 films on RABiTS quenched after various times at 805 °C and then oxygenated at 500 °C for 2 h in pure O_2. The inset shows the superconducting transition zone.

Figure 7 shows the resistance as a function of temperature for samples quenched from 10 to 240 min. The 2 and 5 min samples have very large resistance at room temperature so they are not shown in figure 7. All the samples in figure 7, except the 10 min sample, have optimum oxygen doping, as seen by their straight *R–T* shape above T_c. The 10 min sample appears to be oxygen underdoped. T_c is defined at T_c^{offset} (i.e., where $R \approx 0$, as seen in the inset of figure 7). The inset in figure 7 shows that T_c increases with increasing processing time up to 90 min, and then slowly decreases for longer times.

Figure 8(a) plots J_c–*H* data (*H* ∥ *c*) for samples quenched from 10 to 240 min. J_c increases with increasing processing time up to 90 min at all applied fields then decreases for samples processed for times longer than 90 min. The 90 min sample has the highest J_c in fields up to 5 T and the 60 min sample is the champion in fields greater than 5 T. The volume pinning force F_p is shown in figure 8(b). F_p increases with increasing processing time up to 90 min and then decreases for longer processing times. The decrease of both T_c and J_c for samples processed longer than 90 min at 805 °C might be due to microstructure and texture degradation from the inter-diffusion between YBCO and the buffered RABiTS substrate. The maximum pinning force for the 90 min sample is ∼6.7 GN m^{-3} (*H* ∥ *c*), which is ∼3.5 times greater than for the pure YBCO film. The 60 min sample has the highest irreversibility field of ∼8.1 T (*H* ∥ *c*).

The inset in figure 8(b) is the normalized bulk pinning force, F_p/F_p^{max}, as a function of the reduced field, H/H_{irr} (*H* ∥ *c*) for *x* = 0.10 films processed for different times, as well as for pure YBCO and a single-layer *x* = 0.10 film on STO [24]. Although the magnitude of F_p varies for these samples, it is striking that the shapes of the normalized pinning force curves are identical for all *x* = 0.10 films. It is noteworthy that the peaks for all the normalized pinning force curves for *x* = 0.10 films are shifted to the same, higher normalized magnetic field compared to pure YBCO.
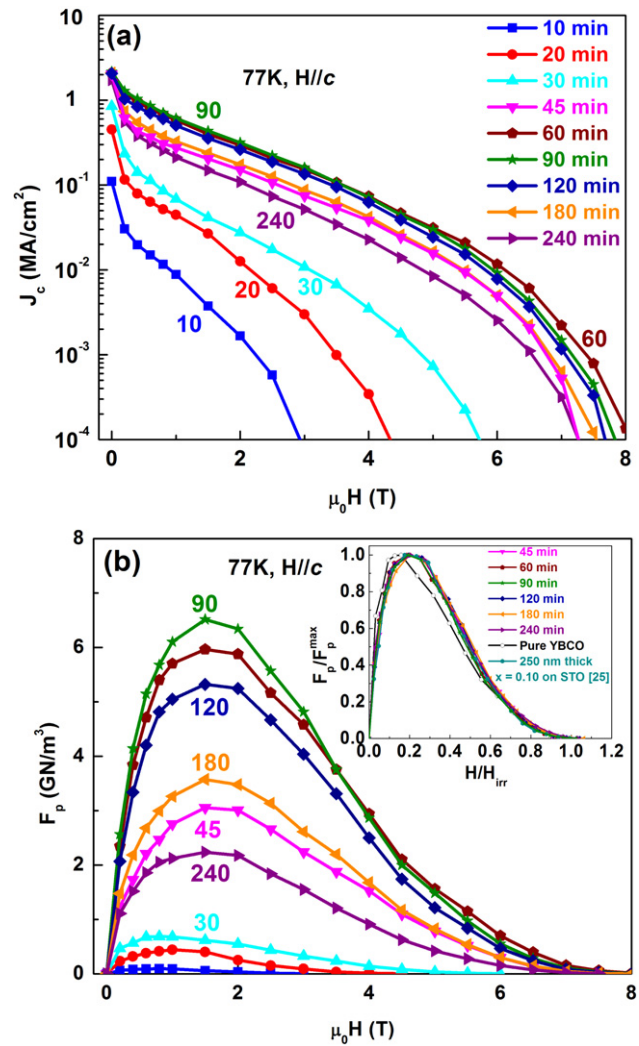

Figure 8. (a) J_c–*H* and (b) F_p–*H* (*H* ∥ *c*) for *x* = 0.10 films on RABiTS quenched at various processing times at 805 °C. The legend is the same for (a) and (b). The inset in (b) shows the normalized bulk pinning force, F_p/F_p^{max}, as a function of reduced field, H/H_{irr}.

3.4. Microstructure of optimally processed film

Figure 9 shows a cross-sectional image TEM of an optimally processed F-free MOD *x* = 0.10 film heated at 805 °C for 90 min. It shows ∼10–25 nm diameter, approximately spherical, dark particles that were identified as BZO by indexing their TEM diffraction patterns. The BZO nanoparticles are spaced 50–100 nm apart and are well dispersed in all directions in the YBCO matrix. In the HRTEM image in figure 9(b), the electron beam is parallel to the YBCO(100) zone axis. Here the YBCO matrix is dark and all the BZO nanoparticles are white. The inset shows an image taken with the electron beam parallel to the (011) BZO planes. Here the contrast is reversed with the BZO nanoparticle being dark and the YBCO matrix white. These two images indicate that there is no particular crystallographic relation between BZO and the YBCO matrix. Therefore BZO is randomly oriented and the interface with
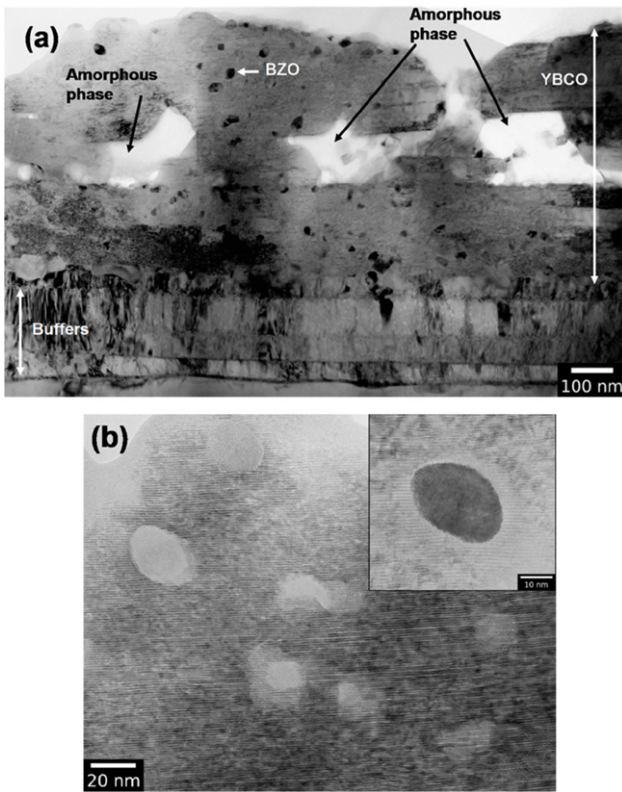
Figure 9. (a) TEM cross-section and (b) high-magnification images of $x = 0.10$ film on RABiTS processed at 805 °C, 90 min. In (b) electron beam is parallel to the YBCO(100) zone axis. The YBCO is dark and the BZO particles are light. In the inset in (b), the electron beam is parallel to (011) in BZO. Here the BZO is dark and the YBCO is light. Taken together these images show that there is no preferred crystallographic orientation between YBCO and BZO.

YBCO is sharp and incoherent in our films. Compared to the microstructures of the single-layer $x = 0.10$ film deposited on single-crystal STO [24], figure 9(a) shows some degradation of the microstructure associated with our F-free MOD multilayer process. In figure 9(a) the bottom YBCO layer is very dense, smooth and well aligned. In the middle part of the YBCO film, several pores and secondary (probably amorphous) phases are present. The top part of YBCO film again appears to be dense, but it has a degraded texture and a rough surface.

3.5. J_c angular dependence of optimally processed film

Figure 10 shows J_c–θ plots of fully processed pure YBCO and $x = 0.10$ films (805 °C, 90 min) at fields of 1 and 4 T. The excellent performance of the $x = 0.10$ film is clear. There is a general increase in the flat background for the $x = 0.10$ film over the entire range of angles at 4 T and most of the range of angles at 1 T. The J_c anisotropy strongly decreases with the BZO doping, indicative of a strong random component in the pinning at 77 K. The ratio of $J_c(H \parallel ab){:}J_c(H \parallel c)$ was used to evaluate the anisotropy. At 1 T the ratio of $J_c(H \parallel ab){:}J_c(H \parallel c)$ is reduced from 9.5 for pure YBCO to 2.5 for the $x = 0.10$ film, and from 16.5 for pure YBCO to 8.0 for the $x = 0.10$ film at 4 T.
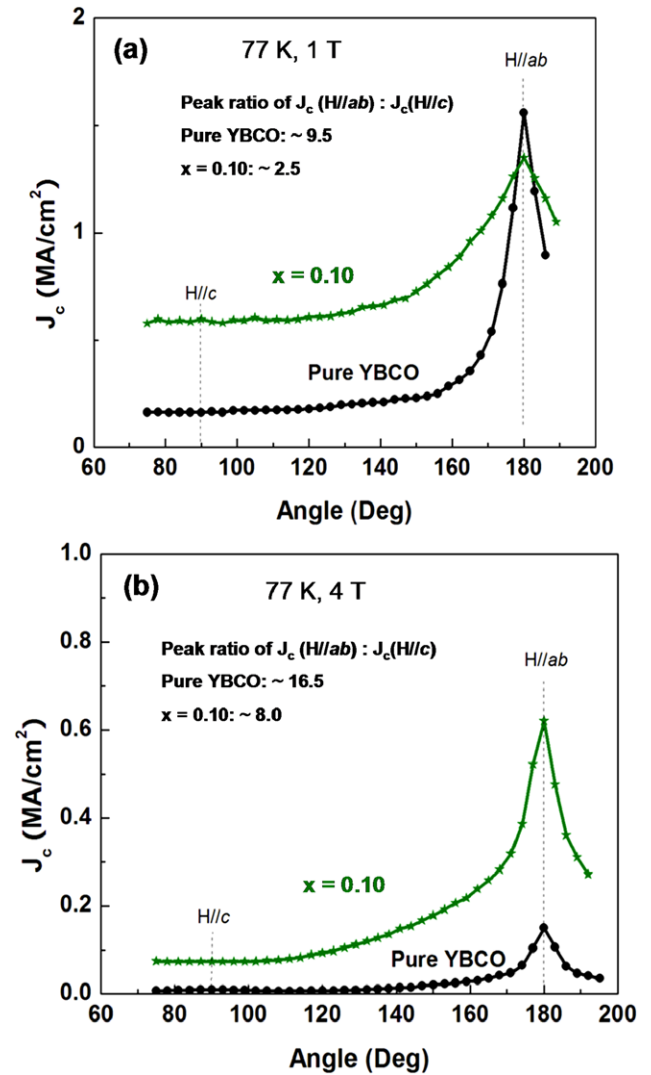

Figure 10. J_c–θ at 77 K, (a) 1 T and (b) 4 T for fully processed pure YBCO and $x = 0.10$ films on RABiTS processed at 805 °C for 90 min.

4. Discussion

The purpose of using the organometallic TFA solutions in the MOD process is to form BaF_2 rather than $BaCO_3$, which is very thermodynamically stable, when CO_2 is released as the organometallic TFA precursors decompose and burn during heating [27]. Recent F-free MOD studies [15–18] investigating the formation of high-J_c YBCO films show that having $BaCO_3$ present as an intermediate phase when forming YBCO films with the AcAc-based MOD process is not a problem. The MOCVD process is also a F-free process, and there are no problems with residual $BaCO_3$ in these fully processed films [28]. Vermeir *et al* [29] reported that $BaCO_3$ is an intermediate phase that reacts with CuO to form $BaCuO_2$ first and this $BaCuO_2$ reacts with the remaining CuO, forming a eutectic liquid that reacts with Y_2O_3 to form YBCO. Although none of the x-ray diffraction patterns of films in this study showed $BaCO_3$ peaks, we speculate that YBCO forms by a similar reaction mechanism involving $BaCO_3$ [29] in our

F-free MOD films and it has fully decomposed by the time the films reach a reaction temperature of 775 °C and above.

Introducing BZO nanoparticles can affect YBCO growth in a F-free MOD process, degrading the microstructure and texture. However, there is little degradation for $x \leq 0.10$ films. The slight T_c reduction from BZO doping listed in table 1 is consistent with other studies done on BZO-doped PLD [23, 30] and TFA-MOD films [5]. The reason for T_c degradation with BZO doping in F-free MOD YBCO is not clear. Nevertheless, it is particularly interesting that J_c (SF) remains almost unchanged for $x = 0$–0.12 even as T_c of these films decreases with increasing BZO content.

Our transport measurements show that introducing BZO nanoparticles can improve in-field J_c in YBCO and the strongest enhancement was achieved with $x = 0.10$. Possible reasons why J_c decreases for $x > 0.10$ are the decrease in T_c, the decrease of YBCO volume fraction, and the degradation of the texture and microstructure, all of which might offset any J_c enhancement due to BZO doping.

For $x = 0.10$ films, increasing the processing temperature by ~20–30 °C over pure YBCO to 795–805 °C can restore or even surpass any negative effect on the film texture due to the BZO doping. The reason the texture improves with increased temperature is that a higher temperature favors the epitaxial nucleation and growth of c-axis films at a lower $p(O_2)$ atmosphere in the AcAc-based MOD process [31]. Our SEM and x-ray patterns show that the increase of J_c for $x = 0.10$ films processed in the 795–805 °C window is associated with the improvement of the texture and microstructure of the film.

The through-process quench experiment reveals that the BZO is already present in the 2 min sample (figure 6) and these BZO grains are stable and do not grow during the heat treatment at 805 °C. Since YBCO and BZO are both present at 2 min, we cannot tell if BZO nucleates before YBCO, but the studies show that YBCO continues to grow during the heat treatment. This is similar to studies of the formation mechanism of BZO nanoparticles in TFA-MOD YBCO films [32, 33]. The overlap of all the normalized bulk pinning force curves for the $x = 0.10$ films with different processing times, seen in the inset of figure 8, implies that these films have similar effective pinning centers in their matrices that are independent of the processing time because the BZO nanoparticles form early and do not grow in size.

TEM shows the BZO nanoparticles are spherical, 10–25 nm in diameter, and uniformly distributed in the $x = 0.10$ film (figure 9). The size and morphology of BZO particles explains the significant increase of in-field J_c as the pin diameter is of the order of 2ξ, where $\xi = 4$ nm is the coherence length of YBCO at 77 K [20].

The TEM image in figure 9(a) shows microstructure degradation associated with the MOD multilayer process. This is, we believe, the main reason that F_p^{max} only reached 6.7 GN m^{-3} ($H \parallel c$) in this 3-layer film compared to 10 GN m^{-3} in our best single-layer $x = 0.10$ film [24]. As a comparison, Miura *et al* [5] achieved a J_c of 3.7 MA cm^{-2} and F_p^{max} of ~7.5 GN m^{-3} at around 1.5–2 T for 1 μm thick 1 wt% BZO-doped Y(Sm)BCO films on IBAD substrates
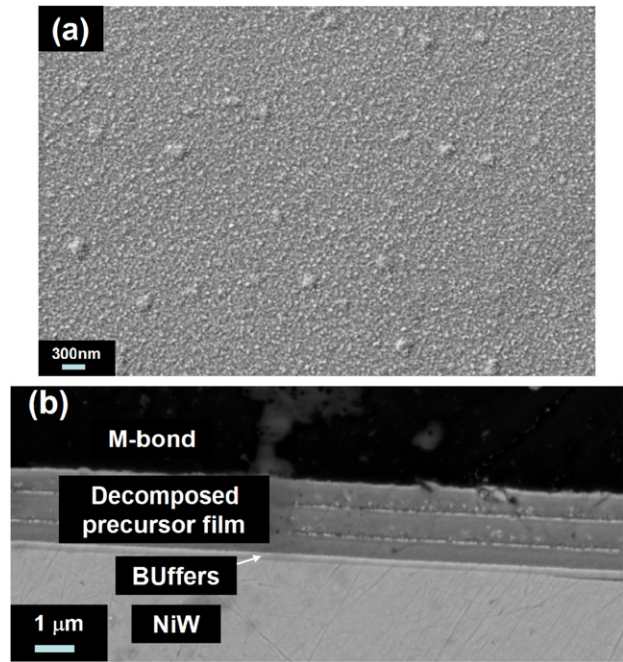

Figure 11. SEM images of an $x = 0.10$ film after the precursors have been decomposed. (a) is the surface of a decomposed precursor layer and (b) shows a cross-section of a 3-layer film.

and Strickland *et al* [2] fabricated ~800 nm thick 10 mol% BZO-doped YBCO films on RABiTS and achieved an I_c of 200–245 A cm^{-1} width (equal to 2.5–3.0 MA cm^{-2}) and F_p^{max} of ~5 GN m^{-3} at around 1.5–2 T. Sathyamuthry *et al* reported a high F_p^{max} exceeding 9 GN m^{-3} on ~800 nm thick TFA-MOD Y(Dy)BCO films with 5% additions of Zr [32] by a modified single-coating approach to minimize the through thickness degradation of microstructure and texture. Similar texture and microstructure degradation are also found in the TFA-MOD [33, 34] and F-free MOD [16] multilayer processes. Those studies show elements and phases segregate to the top of each precursor layer during the decomposition step in both single and multilayer films. In a multilayer process, the chemical segregation at the interface impedes the YBCO growth front, which can result in loss of texture at the interface areas. Figure 11(a) shows the surface of a decomposed precursor layer for an $x = 0.10$ film. The surface is continuous and dense but it has some surface features such as humps and fine particles. The cross-section of a decomposed 3-layer film, shown in figure 11(b), displays some defects, particles and pores at the interface between each layer, which lead to the defects seen in the fully processed film in figure 9(a).

The angular dependence of J_c provides evidence of strongly reduced anisotropy in the $x = 0.10$ film processed at 805 °C for 90 min. The reduced directional anisotropy is expected, because, unlike the self-assembled BZO nanorods formed in PLD YBCO films that are parallel to the c-axis, the spherical BZO nanoparticles are uniformly distributed in the F-free MOD YBCO matrix and can capture fluxons in all magnetic field orientations, which promotes isotropic flux pinning. In the J_c–θ plots (figure 10), the relatively large

peak centered at $H \parallel ab$ is generally caused by intrinsic pinning centers due to the layered crystallographic structure of YBCO and other correlated structures that are parallel to the *ab*-planes. The broadening of the $H \parallel ab$ peak at 1 and 4 T (figure 10) indicates that incoherent BZO nanoparticles also cause extra defects in the *ab*-planes in addition to increasing the isotropic pinning. The small peak centered at $H \parallel c$ is due to the correlated disorder along the *c*-axis, which is smaller in MOD films than in PLD films, which have lots of defects along the *c*-axis, such as twin boundaries, stacking faults and dislocations arising mainly from the columnar grain structure [35].

5. Conclusion

We investigated the effect processing parameters have on the microstructure and superconducting properties of YBCO + x BZO films deposited with an AcAc-based, F-free MOD technique. There exists a compromise between the BZO content and the YBCO matrix texture and microstructure. The maximum J_c is observed at a BZO content of $x = 0.10$. This F-free MOD process was then optimized to grow $x = 0.10$ films on RABiTS substrates. We found that the growth temperature window is ~795–805 °C, which is ~20–30 °C higher than that for pure YBCO, and the optimal processing time in this temperature range is 60–90 min.

The $x = 0.10$ film processed at 805 °C for 90 min has spherical, 10–25 nm diameter, randomly oriented, uniformly distributed, structurally incoherent BZO nanoparticles in the YBCO matrix. These BZO nanoparticles increased the in-field J_c performance by enhancing the flux pinning, reaching ~6.5 GN m^{-3} ($H \parallel c$) in ~800 nm thick YBCO films. The optimally processed $x = 0.10$ films also exhibited a greatly reduced J_c anisotropy at 1 and 4 T compared to pure YBCO films, making them attractive for practical applications in-field at 77 K. The properties of optimally processed F-free MOD $x = 0.10$ films show that the AcAc-based F-free MOD process is an effective way to fabricate high-performance coated conductor on RABiTS substrates.

Acknowledgments

References

[1] Larbalestier D C, Gurevich A, Feldmann D M and Polyanskii A 2001 *Nature* **414** 368–77
[2] Strickland N M, Long N J, Talantsev E F, Hoefakker P, Xia J, Rupich M W, Kodenkandath T, Zhang W, Li X and Huang Y 2008 *Physica* C **468** 183–9
[3] Holesinger T G *et al* 2008 *Adv. Mater.* **20** 391–407
[4] Xu A, Jaroszynski J J, Kametani F, Chen Z, Larbalestier D C, Viouchkov Y L, Chen Y, Xie Y and Selvamanickam V 2010 *Supercond. Sci. Technol.* **23** 014003
[5] Miura M, Kato T, Yoshizumi M, Yamada Y, Izumi T, Shiohara Y and Hirayama T 2008 *Appl. Phys. Express* **1** 051701
[6] Gutierrez J *et al* 2007 *Nature Mater.* **6** 367–73
[7] Xu Y, Goyal A, Leonard K and Martin P 2005 *Physica* C **421** 67–72
[8] Chen Y, Wu C, Zhao G and You C 2012 *Supercond. Sci. Technol.* **25** 062001
[9] Rupich M W, Liu Y P, Ibechem J and Hachey J P 1993 *J. Mater. Res.* **8** 1487–96
[10] Shi D, Xu Y, Yao H, Han Z, Lan J, Wang L, Li A, Liu H K and Dou S X 2004 *Supercond. Sci. Technol.* **17** 1420–5
[11] Cui W, Tanner J L, Button T W and Abell J S 2007 *8th EUCAS* (Belgium: Brussels Expo)
[12] Armenio A A *et al* 2011 *Supercond. Sci. Technol.* **24** 115008
[13] Apetrii C, Schlorb H, Falter M, Lampe I, Schultz L and Holzapfel B 2005 *IEEE Trans. Appl. Supercond.* **15** 2642–4
[14] Wang W T, Pu M H, Wang W W, Zhang H, Cheng C H and Zhao Y 2011 *Physica* C **471** 951–5
[15] Kumagai T, Manabe T, Kondo W, Minamiue H and Mizuta S 1990 *Japan. J. Appl. Phys.* **29** L940–2
[16] Yamaguchi I, Kondo W, Hikata T, Kamiya K, Matsui H, Sohma M, Tsukada K, Nakagawa Y, Kumagai T and Manabe T 2011 *IEEE Trans. Appl. Supercond.* **21** 2775–8
[17] Yamasaki H, Yamaguchi I, Sohma M, Kondo W, Matsui H, Manabe T and Kumagai T 2012 *Physica* C **478** 19–28
[18] Ohmatsu K, Hahakura S, Hasegawa K and Ueyama M 2007 *IEEE Trans. Appl. Supercond.* **17** 3363–6
[19] Lehner T F 2011 2G HTS Wire Status in the USA *ISIS-20: Int. Superconductivity Industry Summit (Gyeonggi-do, South Korea)*
[20] Gurevich A 2007 *Supercond. Sci. Technol.* **20** S128–35
[21] Macmanus-Driscoll J L, Foltyn S R, Jia Q X, Wang H, Serquis A, Civale L, Maiorov B, Hawley M E, Maley M P and Peterson D E 2004 *Nature Mater.* **3** 439–43
[22] Kang S *et al* 2006 *Science* **311** 1911–4
[23] Mele P, Matsumoto K, Horide T, Ichinose A, Mukaida M, Yoshida Y, Horii S and Kita R 2008 *Supercond. Sci. Technol.* **21** 032002
[24] Lu F, Kametani F and Hellstrom E E 2012 *Supercond. Sci. Technol.* **25** 015011
[25] Morlens S, Roma N, Ricart S, Moreto J M, Puig T, Pomar A and Obradors X 2006 *7th EUCAS (Vienna, Austria)*
[26] Wang W T, Li G, Pu M H, Sun R P, Zhou H M, Zhang Y, Zhang H, Yang Y, Cheng C H and Zhao Y 2008 *Physica* C **468** 1563–6
[27] Gupta A, Jagannathan R, Cooper E I, Giess E A, Landman J I and Hussey B W 1988 *Appl. Phys. Lett.* **52** 2077–9
[28] Hatzistergos M S, Efstathiadis H, Reeves J L, Selvamanickam V, Allen L P, Lifshin E and Haldar P 2004 *Physica* C **405** 179–86
[29] Vermeir P, Cardinael I, Schaubroeck J, Verbeken K, Bäcker M, Lommens P, Knaepen W, D'haen J, Buysser K D and Driessche I V 2010 *Inorg. Chem.* **49** 4471–7
[30] Kang S, Goyal A, Li J, Martin P, Ijaduola A, Thompson J R and Paranthaman M 2007 *Physica* C **457** 41–6
[31] Manabe T, Kondo W, Mizuta S and Kumagai T 1991 *Japan. J. Appl. Phys.* **30** L1000–2
[32] Sathyamurthy S, Nguyen D, Coulter Y and Holesinger T 2009 *2009 DOE Annual HTS Program Peer Review* www.htspeerreview.com/2009/pdfs/presentations/day%202/2G/3-LANL-AMSC-CRADA.pdf
[33] Miura M, Yoshizumi M, Izumi T and Shiohara Y 2010 *Supercond. Sci. Technol.* **23** 014013
[34] Miller D, Feenstra R, Holesinger T and Rupich M 2009 *2009 DOE annual HTS Program Peer Review* www.htspeerreview.com/2009/pdfs/presentations/day%201/joint/3-Joint-Wire-Development-Group.pdf
[35] Civale L *et al* 2004 *Appl. Phys. Lett.* **84** 2121–3